

1 **Structure of the mouse TRPC4 ion channel**

2

3 Jingjing Duan<sup>1,2\*</sup>, Jian Li<sup>1,3\*</sup>, Bo Zeng<sup>4\*</sup>, Gui-Lan Chen<sup>4</sup>, Xiaogang Peng<sup>5</sup>, Yixing Zhang<sup>1</sup>,

4 Jianbin Wang<sup>1</sup>, David E. Clapham<sup>2</sup>, Zongli Li<sup>6#</sup>, Jin Zhang<sup>1#</sup>

5

6

7 <sup>1</sup>School of Basic Medical Sciences, Nanchang University, Nanchang, Jiangxi, 330031, China.

8 <sup>2</sup>Howard Hughes Medical Institute, Janelia Research Campus, Ashburn, VA 20147, USA

9 <sup>3</sup>Department of Molecular and Cellular Biochemistry, University of Kentucky, Lexington, KY  
10 40536, USA.

11 <sup>4</sup>Key Laboratory of Medical Electrophysiology, Ministry of Education, and Institute of  
12 Cardiovascular Research, Southwest Medical University, Luzhou, Sichuan, 646000, China

13 <sup>5</sup>The Key Laboratory of Molecular Medicine, the Second Affiliated Hospital of Nanchang  
14 University, Nanchang 330006, China.

15 <sup>6</sup>Howard Hughes Medical Institute, Department of Biological Chemistry and Molecular  
16 Pharmacology, Harvard Medical School, Boston, MA 02115, USA.

17

18 \*These authors contributed equally to this work.

19 # Corresponding authors

20 **Abstract**

21 Members of the transient receptor potential (TRP) ion channels conduct cations into cells. They  
22 mediate functions ranging from neuronally-mediated hot and cold sensation to intracellular  
23 organellar and primary ciliary signaling. Structures belonging to the TRPV, TRPM, TRPP,  
24 TRPA and TRPML subfamilies have been solved, but to date, none of the founding canonical  
25 (TRPC) structures. Here we report an electron cryo-microscopy (cryo-EM) structure of TRPC4  
26 in its apo state to an overall resolution of 3.3 Å. The structure reveals an unusually complex  
27 architecture with a long pore loop stabilized by a disulfide bond. Beyond the shared tetrameric  
28 six-transmembrane fold, the TRPC4 structure deviates from other TRP channels with a unique  
29 cytosolic domain, this unique cytosolic N-terminal domain forms extensive aromatic contacts  
30 with the TRP and the C-terminal domains. The comparison of our structure with other known  
31 TRP structures provides molecular insights into TRPC4 ion selectivity and extends our  
32 knowledge of the diversity and evolution of the TRP channels.

## 33 **Introduction**

34

35 Mammalian transient receptor potential (TRP) channels are activated by a wide spectrum of  
36 signals -- ligands, temperature, lipids, pH -- and as yet unknown stimuli. They are classified into  
37 six subfamilies based on sequence similarity: TRPC (“canonical”), TRPM (“melastatin”), TRPV  
38 (“vanilloid”), TRPA (“ankyrin”), TRPML (“mucolipin”), and TRPP (or PKD) (“polycystin”) (1).

39 The TRPC subfamily are non-selective cation channels ( $\text{Na}^+$ ,  $\text{K}^+$ ,  $\text{Ca}^{2+}$ ) that alter proliferation,  
40 vascular tone, and synaptic plasticity (2, 3). This family can be further subdivided into two  
41 subgroups: TRPC2/3/6/7 and TRPC1/4/5. TRPC4 is broadly expressed in human tissues and can  
42 assemble as homomeric channels or form heteromeric channels with TRPC1 and TRPC5 (4-7).

43 Studies of *Trpc4*-deficient mice have shown that TRPC4 affects endothelial-dependent  
44 regulation of vascular tone, endothelial permeability, and neurotransmitter release from thalamic  
45 interneurons (8). Stimulation of  $G_q$  and  $G_{i/o}$ -G protein coupled receptors (GPCRs) as well as  
46 tyrosine kinase receptors potentiate channel activity (9, 10). Activation is regulated by  
47 intracellular  $\text{Ca}^{2+}$ , phospholipase C, and membrane lipids by unclear mechanisms.

48

49 Along with the revolution in cryo-EM, improved sample preparation, data acquisition, and image  
50 processing strategies, the structures of TRPV1 (11-15), TRPA1 (16), TRPP1(17), TRPML1(18)  
51 and TRPM4 (19-21) have been solved, but to date, no structures of the canonical (TRPC) family  
52 have been published. Here we present the structure of mouse TRPC4 in its apo state at pH 7.5 at  
53 an overall resolution of 3.3 Å.

54

55 **Overall structure of the mouse TRPC4 tetrameric ion channel**

56 The mouse TRPC4 (residues a.a. 1-758, excluding a.a. 759-974) was expressed using the  
57 BacMam expression system (Methods) and purified protein (pH 7.5) was used for single-particle  
58 cryo-EM analysis (**Extended Data Fig. 1a**). The conduction properties of TRPC4 currents were  
59 identical between truncated and full-length constructs, suggesting that our truncated construct  
60 permeates cations (**Extended Data Fig. 1c**).  $\text{Ca}^{2+}$  measurements and electrophysiological  
61 studies were performed to verify that the truncated construct retained sensitivity to channel  
62 activators and blockers, as well as responding to GPCR stimulation (**Extended Data Fig. 1b, c**).  
63 The overall resolution of TRPC4 reconstruction was 3.3 Å (**Extended Data Fig. 2, Table S1**),  
64 which enabled us to construct a near-atomic model (**Extended Data Fig. 3**). Disordered regions  
65 led to poor densities for 4 residues in the S1-S2 loop, 2 residues in the S3-S4 loop, 27 residues in  
66 the distal N terminus, and 28 residues in the truncated distal C terminus. In total, the TRPC4  
67 structure is a four-fold symmetric homotetramer (**Fig. 1a**) with dimensions of 100 Å × 100 Å ×  
68 120 Å (**Fig. 1b**). Each monomer consists of a transmembrane domain (TMD) and a compact  
69 cytosolic domain. The cytosolic domain is composed of two subdomains; the N-terminal  
70 subdomain consisting of four ankyrin repeats (AR1-AR4) and seven  $\alpha$ -helices (H1-H7), and the  
71 C-terminal subdomain containing a connecting helix and a coiled-coil domain (**Fig. 1c, d**).

72

### 73 **Major structural differences with other TRP subfamilies**

74 In **Fig. 2**, we compare the TRPC4 structure with previously reported TRP structures. Not  
75 surprisingly, the organization of 6 helices in each TMD is similar to that of other TRP channels,  
76 while the intracellular architecture is distinct. By superimposing a TRPC4 monomer with  
77 representative TRP monomers from each subfamily, we found that the overall fold of TRPC4 is  
78 closest to that of TRPM4 (**Fig. 2**). TRPC4 has marked similarities to TRPM4 in the TMDs

79 despite their different tissue functions and lack of sequence conservation (<20% identical  
80 residues) (**Extended Data Fig. 4**). Distinctive features of TRPC4 include: 1) the arrangement of  
81 S2-S3 linker, S5, S6, and the pore loop . In TRPC4, the S2-S3 linker is a two-helical turn, shorter  
82 than that of TRPM4 (**Extended Data Fig. 4**), which limits the interactions of S2 and S3 with  
83 their cytoplasmic regions; 2) the disulfide bond between TRPC4's Cys549 and Cys554 lies in the  
84 loop linking S5 and the pore helix (**Fig. 2b, c**), while TRPM4's disulfide bond is located in the  
85 loop between the pore helix and S6. Note that these two cysteines are conserved in TPRC1/4/5,  
86 but not in other TRPC members; 3) a pre-S1 elbow helix connects the N terminus and TMD in  
87 TRPC4 (**Fig. 2d**), as in TRPM4 and NOMPC (19, 22); however, TRPC4 and TRPM4's pre-S1  
88 helix is not found in NOMPC). In TRPC4 the pre-S1 elbow helix directly connects to the pre-S1  
89 helix, while in TRPM4 a characteristic “bridge loop” (approximately 60 residues) connects the  
90 pre-S1 helix with the pre-S1 elbow (**Fig. 2d**).

91

## 92 **Cytosolic domain features and interactions**

93 The cytosolic domains of TRP channels include regulatory components and domain interactions  
94 that may tune channel gating. The cytosolic domain of TRPC4 adopts a pedestal-like architecture  
95 (**Fig. 3a** and **Extended Data Fig. 5a**). The large and unique N-terminal domain of TRPC4  
96 contains a long loop followed by an ankyrin repeat domain (ARD) and helix-loop-helix (HLH)  
97 motifs. These HLH motifs consist of seven helices and several connecting loops (**Fig. 1c, d** and  
98 **Extended Data Fig. 5a**). Similar to TRPM structures, the C-terminal domain of TRPC4 is  
99 composed of two helices, a connecting helix and a coiled-coil domain helix (**Fig. 1c, d**). The  
100 connecting and coiled-coil domain helices bend ~120 degrees to form an inverted “L”  
101 architecture (**Extended Data Fig. 5b**). The coiled-coil domain contains three heptad repeats that

102 exhibit the characteristic periodicity (a-b-c-d-e-f-g)<sub>n</sub> (**Fig. 3 b, c** and **Extended Data Fig. 6**),  
103 with hydrophobic residues at positions “a” and “d”. The presence of Val and Ile at the “a”  
104 position, and Leu and Phe at the “d” position in the core of the coiled-coil domain supports the  
105 formation of a tetramer (**Fig. 3c**).

106

107 Aromatic interactions are important in cytosolic domain arrangements and protein folding (23).  
108 The TRP domain and N-terminal domain interactions are stabilized by  $\pi$ - $\pi$  interactions (formed  
109 by Trp643 with Trp314) and cation- $\pi$  interactions (formed by Phe637 with Lys298; **Fig. 3d, e**).  
110 The N- and C-terminal domains interface is also strengthened by a  $\pi$ - $\pi$  interaction (Tyr271 with  
111 Tyr706) and two hydrogen bonds (Glu264 with Arg716, Arg272 with Arg702) (**Fig. 3d, f**).

112

### 113 **The ion conduction pore, cation and lipids binding sites**

114 Positioned C-terminal to the pore helix, Gly577 marks a restriction point of 6.7 Å between  
115 diagonally opposed residues (Fig. 4 a, b). The corresponding filter-forming residue in TRPM4 is  
116 Gly976 at a 6.0 Å constriction. Compared to TRPM4, TRPC4’s selectivity filter is slightly more  
117 open, but the ion conduction pathway is restricted at its cytoplasmic interface, with Ile617,  
118 Asn621, and Gln625 at the bottom of S6 defining a lower gate. The narrowest constriction of the  
119 ion conduction pathway (3.6 Å) is formed by the S6 side chains of Asn621 (Fig. 4c and  
120 **Extended Data Fig. 7a**), while in TRPM4, the 5.1 Å wide lower gate is positioned at Ile1040  
121 (**Extended Data Fig. 7b**). In contrast, the most restricted point in TRPV1 is in the selectivity  
122 filter (4.8 Å) between opposing Gly643 residues (**Extended Data Fig. 7c**) (24). In TRPA1, the  
123 narrowest point (6.1 Å) is Val961, which is found at its lower gate (16) (**Extended Data Fig. 7d**).  
124 These ~0.5-2.5 Å differences in the narrowest point of TRPs structures may give some clue as to

125 ion selectivity and activation mechanisms, but we also are aware that current resolution  
126 optimization in cryo-EM is still being improved by methods such as model-based local density  
127 sharpening (25), and resolution varies with location within the particle, conditions such as  
128 vitrification, and electron density map fitting.

129 The simplest hypothesis, with these caveats in mind, is that TRPC4 is in a closed or inactivated  
130 state since the lower gate is too narrow to allow the passage of a fully or partially hydrated ion.  
131 In support of this idea is the fact that Gln625 (located in the ion conduction exit pathway) is  
132 conserved in all the TRPC channels, suggesting it plays an important role in ion permeation  
133 (**Extended Data Fig. 8**).

134 TRPC4 is non-selective and thus permeable to monovalents ( $\text{Na}^+$ ,  $\text{K}^+$ ) and some divalents, such  
135 as  $\text{Ca}^{2+}$ . A strong non-protein density peak in our TRPC4 structure is present in a hydrophilic  
136 pocket on the cytoplasmic side of the S1-S4 fold, consistent with the corresponding location of a  
137 presumed  $\text{Ca}^{2+}$  in TRPM4 (**Fig. 4d, e** and **Extended Data Fig. 9**) (19). We tentatively modelled  
138 this non-protein density as  $\text{Na}^+$  since sodium was the most abundant cation in our purification  
139 buffer. The assumed  $\text{Na}^+$  located at the cytoplasmic face is apparently coordinated by side chains  
140 of Glu417 and Gln420 from S2 and the Asp438 and Asn435 from S3 (**Fig. 4e**). The negatively  
141 charged Glu417 and Asp438 are conserved within the TRPC subfamily (except TRPC1)  
142 (**Extended Data Fig. 8**). S1's Tyr373 and the positively charged S4 Arg491 are located above  
143 the cation binding site, forming a lid that may prevent the outward movement of cations (**Fig. 4e**).

144 Eight densities corresponding to lipid molecules were clearly resolved and identified as  
145 cholesteryl hemisuccinates (CHS) and phospholipids (the density fitting ceramide-1-phosphate  
146 or phosphatidic acid) (**Extended Data Fig. 3** and **Extended Data Fig. 10**). Four CHS located at  
147 the interface of the N-terminal domain and the S4/S5 linker are bound to each protomer,

148 stabilizing the domain interaction (**Extended Data Fig. 10**). The phospholipid is embedded in  
149 the gap between the 4 monomeric subunits with its polar head interacting with the pore helix and  
150 neighboring S6 helix (**Extended Data Fig. 10**). In vivo phosphorylation or dephosphorylation of  
151 membrane lipids could thus alter the topology of the ion conduction pathway.

152 The TRPC4 structure provides a detailed view of the core domain of the canonical TRPC  
153 subfamily. Along with the other recent TRP structures, we now have general structural principles  
154 of this family of proteins. Comparison with other TRP channel structures highlights some  
155 commonalities and differences. Not surprisingly, all TRP channels are tetramers with domain  
156 swapping interactions, pore loops, selectivity filters, and extracellular and intracellular-facing  
157 constriction sites, as first shown for 6 TM K<sup>+</sup> channels (26). One interesting feature that bears  
158 functional investigation is the extracellular pore loop disulfide bond (e.g., TRPC4 and TRPM4).  
159 Interestingly, the lower gate in the TRPC4 appears to have an unusual set of three constriction  
160 sites not found in other TRP channel structures. An ion binding site located in the hydrophilic  
161 binding pocket in the S1-S4 domain is observed in TRPC4 and TRPM4, which may be a general  
162 feature of these two subfamilies. We suspect that the most interesting differences between TRP  
163 channels lies in their less well structurally and functionally characterized extracellular and  
164 intracellular domains. These areas are best suited to ligand interactions that alter gating and  
165 drive the evolution of the ~30 TRP channel members.

166

## 167 **Materials and Methods**

168 **Protein expression and purification.** The mouse TRPC4 construct (a.a. 1-758 of 974), was  
169 cloned into the pEG BacMam vector (27) and a maltose binding protein (MBP) tag was added to  
170 its N terminus. P3 baculovirus were produced in the Bac-to-Bac Baculovirus Expression System



171 (Invitrogen). HEK293S GnTII<sup>-</sup> cells were infected with 10% (v/v) P3 baculovirus at a density of  
172  $2.0 - 3.0 \times 10^6$  cells/ml for protein expression at 37°C. After 12-24 h, 10 mM sodium butyrate  
173 was added and the temperature reduced to 30°C. Cells were harvested at 72 h after transduction,  
174 and resuspended in a buffer containing 30 mM HEPES, 150 mM NaCl, 1 mM dithiothreitol  
175 (DTT), pH 7.5 with EDTA-free protease inhibitor cocktail (Roche). After 30 min, cells were  
176 solubilized for 2-3 h in a buffer containing 1.0 % (w/v) N-dodecyl-beta-D-maltopyranoside  
177 (DDM, Affymetrix), 0.1% (w/v) cholesteryl hemisuccinate (CHS, Sigma), 30 mM HEPES, 150  
178 mM NaCl, 1 mM DTT; pH 7.5 with EDTA-free protease inhibitor cocktail (Roche). The  
179 supernatant was isolated by 100,000×g centrifugation for 60 min, followed by incubation in  
180 amylose resin (New England BioLabs) at 4°C overnight. The resin was washed with 20 column  
181 volumes of ‘washing buffer’ containing 25 mM HEPES, 150 mM NaCl, 0.1% (w/v) digitonin,  
182 0.01% (w/v) CHS, 1 mM DTT; pH 7.5 with EDTA-free protease inhibitor cocktail (Roche). The  
183 protein was eluted with 4 column volumes of washing buffer with 40 mM maltose. The protein  
184 was then concentrated to 0.5 ml with a 100 kDa molecular weight cut-off concentrator  
185 (Millipore). PreScission protease was added to the samples and incubated overnight at 4°C to  
186 remove the MBP tag. After incubation at 4°C overnight, the protein was then purified on a  
187 Superose 6 column in a buffer composed of 25 mM HEPES, 150 mM NaCl, 0.1% (w/v)  
188 digitonin, 1 mM DTT; pH 7.5. The peak, corresponding to tetrameric TRPC4 was collected and  
189 concentrated to 4.5 mg/ml for cryo-EM study.

190 **Electron microscopy data collection.** Purified TRPC4 protein (3.5 µl) in digitonin at 4.5 mg/ml  
191 was applied onto a glow-discharged, 400 mesh copper Quantifoil R1.2/1.3 holey carbon grid  
192 (Quantifoil). Grids were blotted for 7 s at 100% humidity and flash frozen by liquid nitrogen-  
193 cooled liquid ethane using a FEI Vitrobot Mark I (FEI). The grid was then loaded onto an FEI

194 TF30 Polara electron microscope operated at 300 kV accelerating voltage. Image stacks were  
195 recorded on a Gatan K2 Summit (Gatan) direct detector set in super-resolution counting mode  
196 using SerialEM (28), with a defocus range between 1.5 to 3.0  $\mu\text{m}$ . The electron dose was set to 8  
197  $\text{e}^-/\text{physical pixel/s}$  and the sub-frame time to 200 ms. A total exposure time of 10 s resulted in 50  
198 sub-frames per image stack. The total electron dose was 52.8  $\text{e}^-$  per  $\text{\AA}^2$  ( $\sim 1.1 \text{e}^-$  per  $\text{\AA}^2$  per sub-  
199 frame).

200 **Image processing and 3D reconstruction.** Image stacks were gain-normalized and binned by  
201 2x to a pixel size of 1.23  $\text{\AA}$  prior to drift and local movement correction using motionCor2 (29).  
202 The images from the sum of all frames with dose-weighting were subjected to visual inspection  
203 and poor images were removed before particle picking. Particle picking and subsequent bad  
204 particle elimination through 2D classification was performed using Python scripts/programs (30)  
205 with minor modifications in the 8x binned images. The selected 2D class averages were used to  
206 build an initial model using the common lines approach implemented in SPIDER (31) through  
207 Maofu Liao's Python scripts (30), which was applied to later 3D classification using RELION  
208 (32). Contrast transfer function (CTF) parameters were estimated using *CTFFIND4* (33) using  
209 the sum of all frames without dose-weighting. Quality particle images were then boxed out from  
210 the dose-weighted sum of all 50 frames and subjected to RELION 3D classification. RELION  
211 3D refinements were then performed on selected classes for the final map. The resolution of this  
212 map was further improved by using the sum of sub-frames 1-14.

213 **Model building, refinement and validation.** For the TRPC4, a polyalanine model was first  
214 built in COOT (34). Taking advantage of the defined geometry of helices and clear bumps for  
215  $\text{C}\alpha$  atoms in the transmembrane domain, amino acid assignment was subsequently achieved  
216 based primarily on the clearly defined side chain densities of bulky residues. The refined atomic

217 model was further visualized in COOT. A few residues with side chains moving out of the  
218 density during the refinement were fixed manually, followed by further refinement. The TRPC4  
219 model was then subjected to global refinement and minimization in real space using the PHENIX  
220 (35) module ‘phenix.real\_space\_refine’(36) and geometry of the model was assessed using  
221 MolProbity (37) in the comprehensive model validation section of PHENIX. The final model  
222 exhibited good geometry as indicated by the Ramachandran plot (preferred region, 97.39%;  
223 allowed region, 2.08%; outliers, 0.53%). The pore radius was calculated using HOLE (38).

## 224 **Electrophysiology and Ca<sup>2+</sup> measurements**

225 TRPC4 constructs or empty vector were transfected into 293T cells together with an mCherry  
226 plasmid. Cells with red fluorescence were selected for whole-cell patch recordings (HEKA  
227 EPC10 USB amplifier, Patchmaster 2.90 software). A 1-s ramp protocol from –100 mV to +100  
228 mV was applied at a frequency of 0.2 Hz. Signals were sampled at 10 kHz and filtered at 3 kHz.  
229 The pipette solution contained (mM): 140 CsCl, 1 MgCl<sub>2</sub>, 0.03 CaCl<sub>2</sub>, 0.05 EGTA, 10 HEPES,  
230 and the pH was titrated to 7.2 using CsOH. The standard bath solution contained (mM): 140  
231 NaCl, 5 KCl, 1 MgCl<sub>2</sub>, 2 CaCl<sub>2</sub>, 10 HEPES, 10 D-Glucose, and the pH was adjusted to 7.4 with  
232 NaOH. The recording chamber had a volume of 150 µl and was perfused at a rate of ~2 ml/min.  
233 For Ca<sup>2+</sup> imaging experiments, transfected 293T cells were seeded on coverslips and incubated  
234 with Fura-2 AM (2 µM) for 30 min at 37°C in standard bath solution. The ratio (F<sub>340</sub>/F<sub>380</sub>) of  
235 Ca<sup>2+</sup> dye fluorescence was measured by a Nikon Ti-E system with NIS-Elements software. All  
236 the experiments were performed at room temperature.

237

## 238 **Acknowledgements**

239 We thank Dr. Steve Harrison and the Cryo-EM Facility (Harvard Medical School) for use of  
240 their microscopes. We thank Dr. Maofu Liao for providing the Python scripts and help in image  
241 processing. We thank Dr. Corey Valinsky's help on manuscript revision. J.Z. was supported by  
242 the Thousand Young Talents Program of China and National Natural Science Foundation of  
243 China (Grant No. 31770795). J.L. was supported by the National Natural Science Foundation of  
244 China (Grant No. 81402850). Functional studies in this project were supported by the National  
245 Natural Science Foundation of China (31300949 to B.Z. and 31300965 to G.L.C.)

246

#### 247 **Author Contributions**

248 J.Z. and J.D. designed and made constructs for BacMam expression and determined the  
249 condition to enhance protein stability. J.Z. purified the protein. Z.L. carried out detailed cryo-EM  
250 experiments, including data acquisition and processing. J.L., and J.Z. built the atomic model on  
251 the basis of cryo-EM maps. B.Z. and G.L.C. performed functional studies. X. P., Y.Z. and J.W.  
252 assisted with protein purification and the mutation of TRPC4 constructs for functional studies.  
253 J.D. and J.Z. drafted the initial manuscript. All authors contributed to structure  
254 analysis/interpretation and manuscript revision. J.Z. and Z.L. initiated the project, planned and  
255 analyzed experiments and supervised the research.

256

257 The authors declare no competing financial interests.

258 Data deposition: Cryo-EM electron density map of the mouse TRPC4 has been deposited in the  
259 Electron Microscopy Data Bank, <https://www.ebi.ac.uk/pdbe/emdb/> (accession number EMD-  
260 6901), and the fitted coordinate has been deposited in the Protein Data  
261 Bank, [www.pdb.org](http://www.pdb.org) (PDB ID code 5Z96).

262 **Figure legends**

263 **Figure 1: Overall structure of mTRPC4.**

264 **a**, Side and top views of cryo-EM density map of mouse TRPC4 at 3.3 Å overall resolution.  
265 Each monomer is represented in different colors. **b**, Ribbon diagrams of the mouse TRPC4  
266 model with channel dimensions indicated. **c**, Ribbon diagrams depicting structural details of a  
267 single subunit. **d**, Linear diagram depicting the major structural domains of the TRPC4 monomer,  
268 color-coded to match the ribbon diagram in **c**.

269

270 **Figure 2: Comparison of the TRPC4 structure with previously solved TRP channel**  
271 **structures (apo state)**

272 **a**, Side views of an mTRPC4 subunit compared with other TRP family members including  
273 human TRPM4 (PDB: 6BWI)(20), mouse TRPV1 (PDB: 3J5P)(13), human TRPA1 (PDB:  
274 3J9P)(16), human PKD2/TRPP1 (PDB: 5T4D)(17), and mouse TRPML1 (PDB: 5WPV)(18). **b**,  
275 Superimposition of TRPC4 and TRPM4. **c**, Key pore loop-disulfide bond between Cys549 and  
276 Cys554 in TRPC4 and the corresponding pore loop-disulfide bond between Cys993 and Cys1011  
277 in TRPM4 (Black arrows); **d**, Differences in the organizations of the linker (pre-S1 elbow and  
278 pre-S1 helix) between the N terminus and transmembrane domains in TRPC4 and TRPM4.

279

280 **Figure 3. Unique cytosolic domains and interactions**

281 **a**, Side and top views of the cytosolic domains including full-length N- and truncated C-terminal  
282 domains. **b**, Ribbon diagram of the tetrameric coiled-coil domain structure. Side chains are  
283 represented by ball and stick models. **c**, Helical wheel projection of the residues in the coiled-coil  
284 domain of TRPC4. **d**, Side views of a single subunit of the N-terminal domain to illustrate the

285 locations of the interactions between the **e**, TRP domain (*Blue*) and N-terminal domain (*orange*)  
286 and **f**, N-terminal domain (*orange*) and truncated C-terminal domain (*purple*).

287

288 **Figure 4. TRPC4 ion conduction pathway**

289 **a**, Ion conduction pathway shown as dots and mapped using HOLE. **b**, Pore radius along the  
290 central axis. The side chains of G577 form a narrow constriction at the selectivity filter. N621 is  
291 the most restricted site of the lower gate. The dashed line represents TRPM4 for comparison. **c**,  
292 Side view of TRPC4's pore region with chains A and C. The distances between diagonal  
293 residues in the selectivity filter and lower gate are labeled. **d**, A putative Na<sup>+</sup> is found on the  
294 cytosolic side in the hydrophilic pocket of the S1-S4 domain interacting with E417, Q420, N435  
295 and D438 (orange sphere). **e**, Enlarged view of second putative Na<sup>+</sup> binding site.

296

297

298 **Extended Data Figure**

299

300 **Extended Data Figure 1. The TRPC4 construct encodes a functional channel; biochemical**  
301 **characterization.**

302 **a**, Size exclusion chromatography trace of TRPC4 proteins. Void volume ( $V_0$ ) and the peaks  
303 corresponding to tetrameric TRPC4 and MBP are indicated. Protein samples of the indicated  
304 TRPC4 protein fraction were subjected to SDS-PAGE and Coomassie-blue staining. **b**,  
305 Intracellular  $Ca^{2+}$  measurements as indicated by Fura-2 AM (2  $\mu$ M). **c**, Representative whole-cell  
306 patch clamp recordings and *I-V* relationships of truncated mTRPC4, full-length mTRPC4, and  
307 empty vector expressed in HEK293T cells. TRPC4 sensitivity to the activator Englerin A,  
308 blockers ML204 and 2-APB, and the GPCR agonist trypsin was not affected by truncation.

309

310 **Extended Data Figure 2. Flow chart for cryo-EM data processing of the TRPC4 structure.**

311 **a**, Representative image of the purified TRPC4 protein, 2D class averages of TRPC4 particles,  
312 side views of the 3D reconstructions from RELION 3D classification and final 3D  
313 reconstructions from 3D auto-refinement. **b**, Fourier shell correlation (FSC) curve for the 3D  
314 reconstruction (marked at overall 3.3 Å resolution). **c**, Local resolution estimation from ResMap  
315 (39) and **d**, Euler distribution plot of particles used in the final three-dimensional reconstruction.  
316 The length of the rod is proportional to the number of particles in that view, with regions in red  
317 denoting the views containing the highest number of particles.

318

319 **Extended Data Figure 3. Cryo-EM densities of selected regions of TRPC4.**

320 Density map showing the transmembrane helices (S1-S6), an ankyrin repeat (AR), N-terminal  
321 helix, TRP domain, pore helix, connecting helix, coiled-coil helix, and lipids. The maps were  
322 contoured at a level of  $3.0 \sigma$ .

323

324 **Extended Data Figure 4. Comparison of the 6 transmembrane domain structures of**  
325 **TRPC4 and TRPM4.**

326 Side (left) and top (right) views of the channel transmembrane domain monomers of two  
327 channels were overlapped for comparison. The helices of the apo states of TRPC4 (blue) and  
328 TRPM4 (orange) adopt a similar conformation in S1-S4, but differ in the S2-S3 linker and the  
329 orientation of S5 and S6.

330

331 **Extended Data Figure 5. Cytosolic domains of the TRPC4 monomer.**

332 Side views of the **a**, N-terminal and **b**, truncated C-terminal domains.

333

334 **Extended Data Figure 6. The three heptad repeats of the coiled-coil domain.**

335 **a**, Side and top views of the periodic region of the coiled-coil domain denoted as (a-b-c-d-e-f-g)<sub>n</sub>;

336 **b**, Protein sequences of conserved coiled-coil domain of TRPC4 and TRPC5. Residues included

337 in TRPC4 and TRPC5 are indicated in black. Residues at positions “a” and “d” are shown in red.

338

339 **Extended Data Figure 7. Comparison of ion conducting pathway in TRP family.**

340 Comparison of ion conduction pathway openings of **a**, TRPC4, **b**, TRPM4 (PDB: 6BWI), **c**,

341 TRPV1 (PDB: 3J5P) and **d**, TRPA1 (PDB: 3J9P). Distances between specific side chains along

342 the pore and the key residues are labeled.



343

344 **Extended Data Figure 8. Sequence alignment of TRPC subfamily members.**

345 Sequence of the full-length mouse TRPC4 aligned to other TRPC subfamily members are shown;  
346 key residues indicated. Regions corresponding to putative Na<sup>+</sup> binding sites are labeled. The  
347 selectivity filter, lower gate, and two cysteines forming disulfide bonds are highlighted.  
348 Sequence alignments of this study were performed using Clustal Omega.

349

350 **Extended Data Figure 9. Electrostatic maps of the predicted Na<sup>+</sup> binding sites.**

351 Side and top views of electrostatic maps of predicted Na<sup>+</sup> binding pockets in TRPC4; **a**,  
352 monomer and **b**, tetramer. The surface is colored according to the calculated electrostatic  
353 potential. The electrostatics reveal the tetrameric distribution of charge. Blue indicates positive  
354 potential, red negative, and transparent white neutral.

355

356 **Extended Data Figure 10. Lipid coordination in TRPC4.**

357 **a**, Side and top views of ribbon diagrams of the TRPC4 tetramer: 4 cholesterol hemisuccinate  
358 (CHS) molecules and 4 phospholipids (potentially ceramide-1-phosphate, C1P, or phosphatidic  
359 acid, PA) shown in cyan. **b**, Side views of each CHS and PA molecules per protomer. **c** and **d**,  
360 Ribbon diagram of the TRPC4 lipids binding. **c**, CHS, shown in cyan, interacts with the S4/S5  
361 linker and Tyr315 in the N-terminal domain. **d**, PA is imbedded in the gap between the pore  
362 helix and neighboring subunit and interacts with the head groups of Gln569, Trp573, and Ala598.  
363 **e**. Side view of the electrostatic map around the putative PA binding pocket. The surface is  
364 colored according to the calculated electrostatic potential, revealing the tetrameric distribution of  
365 charge. Blue shows positive potential, red negative, and transparent white neutral.

366

367 References

- 368 1. Clapham DE (2003) TRP channels as cellular sensors. *Nature* 426(6966):517-524.
- 369 2. Selvaraj S, Sun Y, & Singh BB (2010) TRPC channels and their implication in  
370 neurological diseases. *CNS Neurol Disord Drug Targets* 9(1):94-104.
- 371 3. Gees M, Colsoul B, & Nilius B (2010) The role of transient receptor potential cation  
372 channels in Ca<sup>2+</sup> signaling. *Cold Spring Harb Perspect Biol* 2(10):a003962.
- 373 4. Strubing C, Krapivinsky G, Krapivinsky L, & Clapham DE (2003) Formation of novel  
374 TRPC channels by complex subunit interactions in embryonic brain. *J Biol Chem*  
375 278(40):39014-39019.
- 376 5. Strubing C, Krapivinsky G, Krapivinsky L, & Clapham DE (2001) TRPC1 and TRPC5  
377 form a novel cation channel in mammalian brain. *Neuron* 29(3):645-655.
- 378 6. Zhu X, *et al.* (1996) trp, a novel mammalian gene family essential for agonist-activated  
379 capacitative Ca<sup>2+</sup> entry. *Cell* 85(5):661-671.
- 380 7. Clapham DE, Julius D, Montell C, & Schultz G (2005) International Union of  
381 Pharmacology. XLIX. Nomenclature and structure-function relationships of transient  
382 receptor potential channels. *Pharmacological Reviews* 57(4):427-450.
- 383 8. Freichel M, *et al.* (2004) Functional role of TRPC proteins in vivo: lessons from TRPC-  
384 deficient mouse models. *Biochem Biophys Res Commun* 322(4):1352-1358.
- 385 9. Schaefer M, *et al.* (2000) Receptor-mediated regulation of the nonselective cation  
386 channels TRPC4 and TRPC5. *Journal of Biological Chemistry* 275(23):17517-17526.
- 387 10. Thakur DP, *et al.* (2016) Critical roles of Gi/o proteins and phospholipase C-delta1 in the  
388 activation of receptor-operated TRPC4 channels. *Proc Natl Acad Sci U S A* 113(4):1092-  
389 1097.
- 390 11. Hughes TET, *et al.* (2018) Structural basis of TRPV5 channel inhibition by econazole  
391 revealed by cryo-EM. *Nat Struct Mol Biol* 25(1):53-60.
- 392 12. Gao Y, Cao E, Julius D, & Cheng Y (2016) TRPV1 structures in nanodiscs reveal  
393 mechanisms of ligand and lipid action. *Nature* 534(7607):347-351.
- 394 13. Liao M, Cao E, Julius D, & Cheng Y (2013) Structure of the TRPV1 ion channel  
395 determined by electron cryo-microscopy. *Nature* 504(7478):107-112.
- 396 14. Huynh KW, *et al.* (2016) Structure of the full-length TRPV2 channel by cryo-EM. *Nat*  
397 *Commun* 7:11130.
- 398 15. McGoldrick LL, *et al.* (2018) Opening of the human epithelial calcium channel TRPV6.  
399 *Nature* 553(7687):233-237.
- 400 16. Paulsen CE, Armache JP, Gao Y, Cheng Y, & Julius D (2015) Structure of the TRPA1  
401 ion channel suggests regulatory mechanisms. *Nature* 520(7548):511-517.
- 402 17. Shen PS, *et al.* (2016) The Structure of the Polycystic Kidney Disease Channel PKD2 in  
403 Lipid Nanodiscs. *Cell* 167(3):763-773 e711.
- 404 18. Chen Q, *et al.* (2017) Structure of mammalian endolysosomal TRPML1 channel in  
405 nanodiscs. *Nature*.
- 406 19. Autzen HE, *et al.* (2018) Structure of the human TRPM4 ion channel in a lipid nanodisc.  
407 *Science* 359(6372):228-232.
- 408 20. Duan, J. *et al.* (2018) Structure of full-length human TRPM4. *Proc Natl Acad Sci U S A*  
409 115, 2377-2382.

- 410 21. Guo J, *et al.* (2017) Structures of the calcium-activated, non-selective cation channel  
411 TRPM4. *Nature* 552(7684):205-209.
- 412 22. Jin P, *et al.* (2017) Electron cryo-microscopy structure of the mechanotransduction  
413 channel NOMPC. *Nature* 547(7661):118-122.
- 414 23. Meyer EA, Castellano RK, & Diederich F (2003) Interactions with aromatic rings in  
415 chemical and biological recognition. *Angew Chem Int Ed Engl* 42(11):1210-1250.
- 416 24. Cao E, Liao M, Cheng Y, & Julius D (2013) TRPV1 structures in distinct conformations  
417 reveal activation mechanisms. *Nature* 504(7478):113-118.
- 418 25. Jakobi AJ, Wilmanns M, & Sachse C (2017) Model-based local density sharpening of  
419 cryo-EM maps. *Elife* 6.
- 420 26. Long SB, Campbell EB, & Mackinnon R (2005) Crystal structure of a mammalian  
421 voltage-dependent Shaker family K<sup>+</sup> channel. *Science* 309(5736):897-903.
- 422 27. Goehring A, *et al.* (2014) Screening and large-scale expression of membrane proteins in  
423 mammalian cells for structural studies. *Nat Protoc* 9(11):2574-2585.
- 424 28. Mastronarde DN (2005) Automated electron microscope tomography using robust  
425 prediction of specimen movements. *Journal of Structural Biology* 152(1):36-51.
- 426 29. Zheng SQ, *et al.* (2017) MotionCor2: anisotropic correction of beam-induced motion for  
427 improved cryo-electron microscopy. *Nat Methods* 14(4):331-332.
- 428 30. Ru H, *et al.* (2015) Molecular Mechanism of V(D)J Recombination from Synaptic  
429 RAG1-RAG2 Complex Structures. *Cell* 163(5):1138-1152.
- 430 31. Frank J, *et al.* (1996) SPIDER and WEB: Processing and visualization of images in 3D  
431 electron microscopy and related fields. *Journal of Structural Biology* 116(1):190-199.
- 432 32. Scheres SH (2012) RELION: implementation of a Bayesian approach to cryo-EM  
433 structure determination. *J Struct Biol* 180(3):519-530.
- 434 33. Rohou A & Grigorieff N (2015) CTFIND4: Fast and accurate defocus estimation from  
435 electron micrographs. *J Struct Biol* 192(2):216-221.
- 436 34. Emsley P, Lohkamp B, Scott WG, & Cowtan K (2010) Features and development of  
437 Coot. *Acta Crystallogr D Biol Crystallogr* 66(Pt 4):486-501.
- 438 35. Adams PD, *et al.* (2010) PHENIX: a comprehensive Python-based system for  
439 macromolecular structure solution. *Acta Crystallogr D Biol Crystallogr* 66(Pt 2):213-221.
- 440 36. Afonine PV, Headd JJ, Terwilliger TC, & Adams PD (2013) New tool:  
441 phenix.real\_space\_refine. *Computational Crystallography Newsletter*  
442 4:43-44.
- 443 37. Chen VB, *et al.* (2010) MolProbity: all-atom structure validation for macromolecular  
444 crystallography. *Acta Crystallogr D Biol Crystallogr* 66(Pt 1):12-21.
- 445 38. Smart OS, Neduvilil JG, Wang X, Wallace BA, & Sansom MS (1996) HOLE: a program  
446 for the analysis of the pore dimensions of ion channel structural models. *J Mol Graph*  
447 14(6):354-360, 376.
- 448 39. Kucukelbir A, Sigworth FJ, & Tagare HD (2014) Quantifying the local resolution of  
449 cryo-EM density maps. *Nat Methods* 11(1):63-65.
- 450

**Figure 1.**

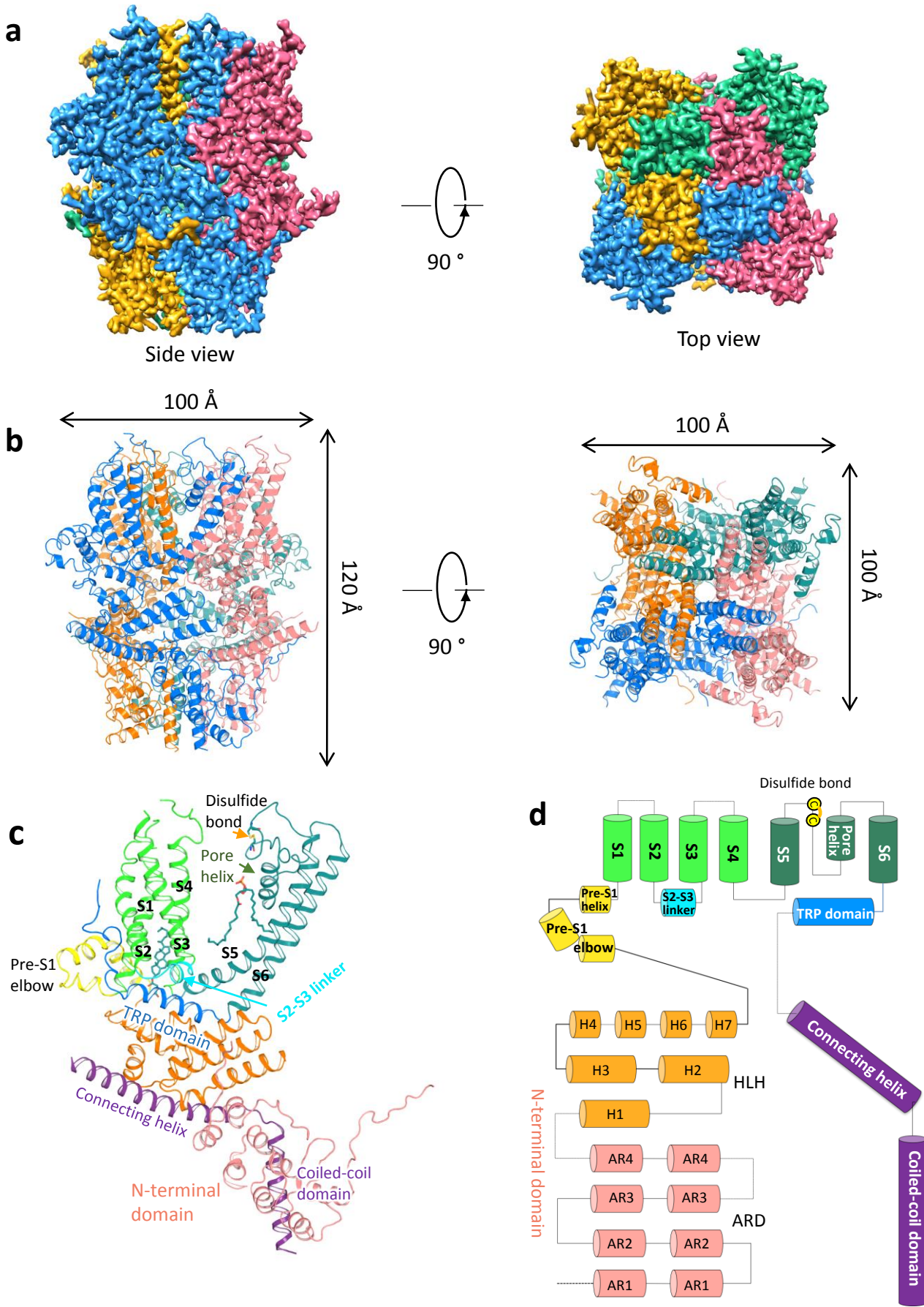




**Figure 2.**

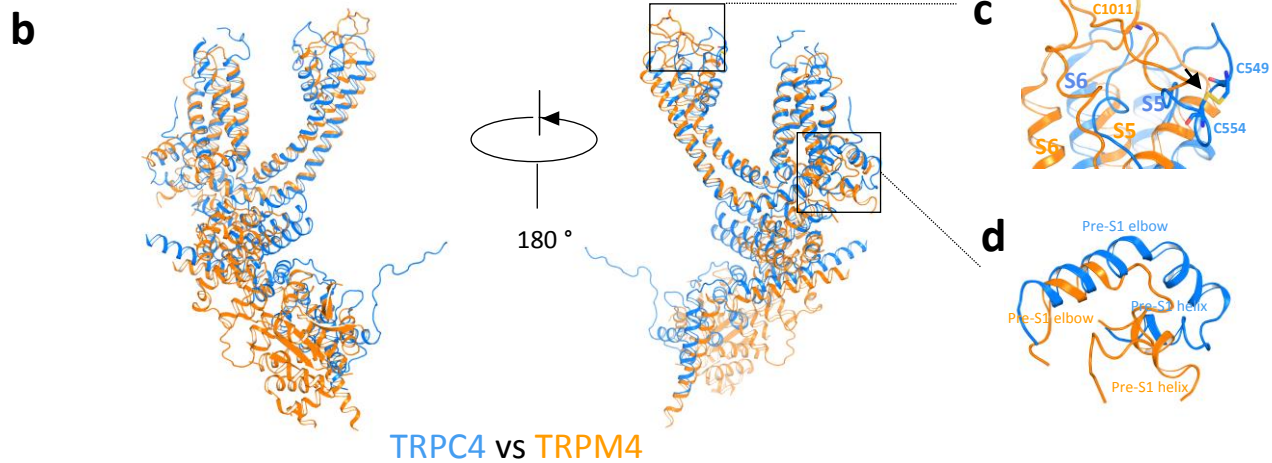
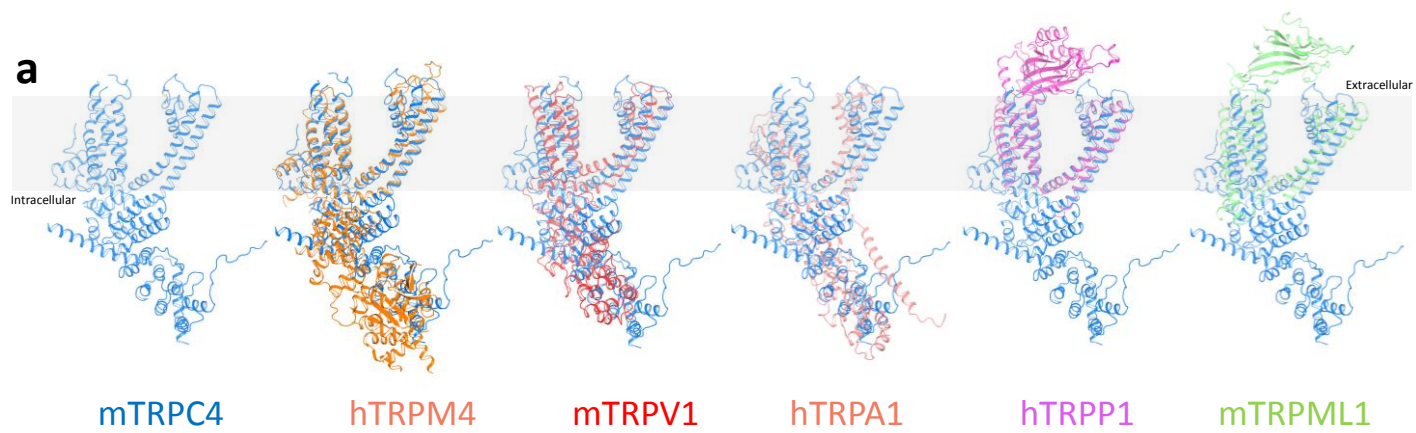


**Figure 3.**

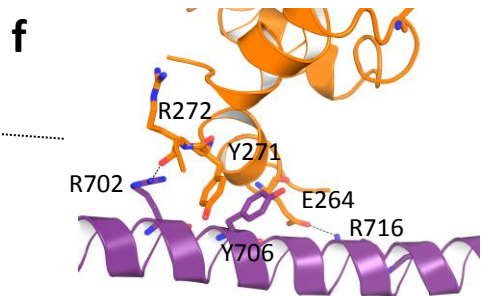
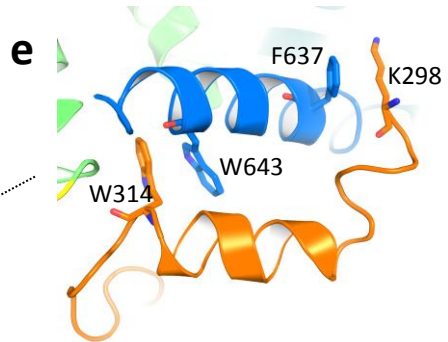
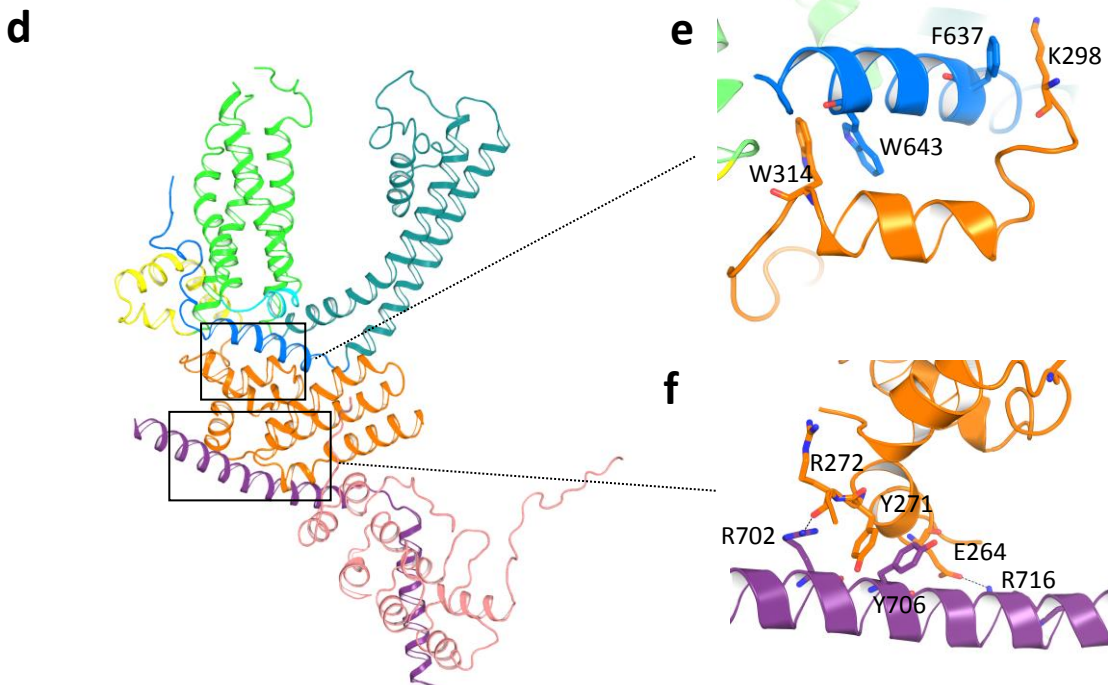
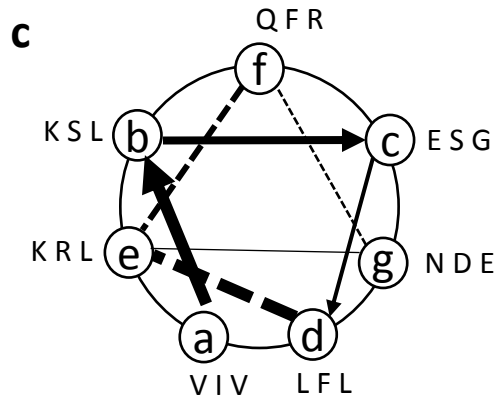
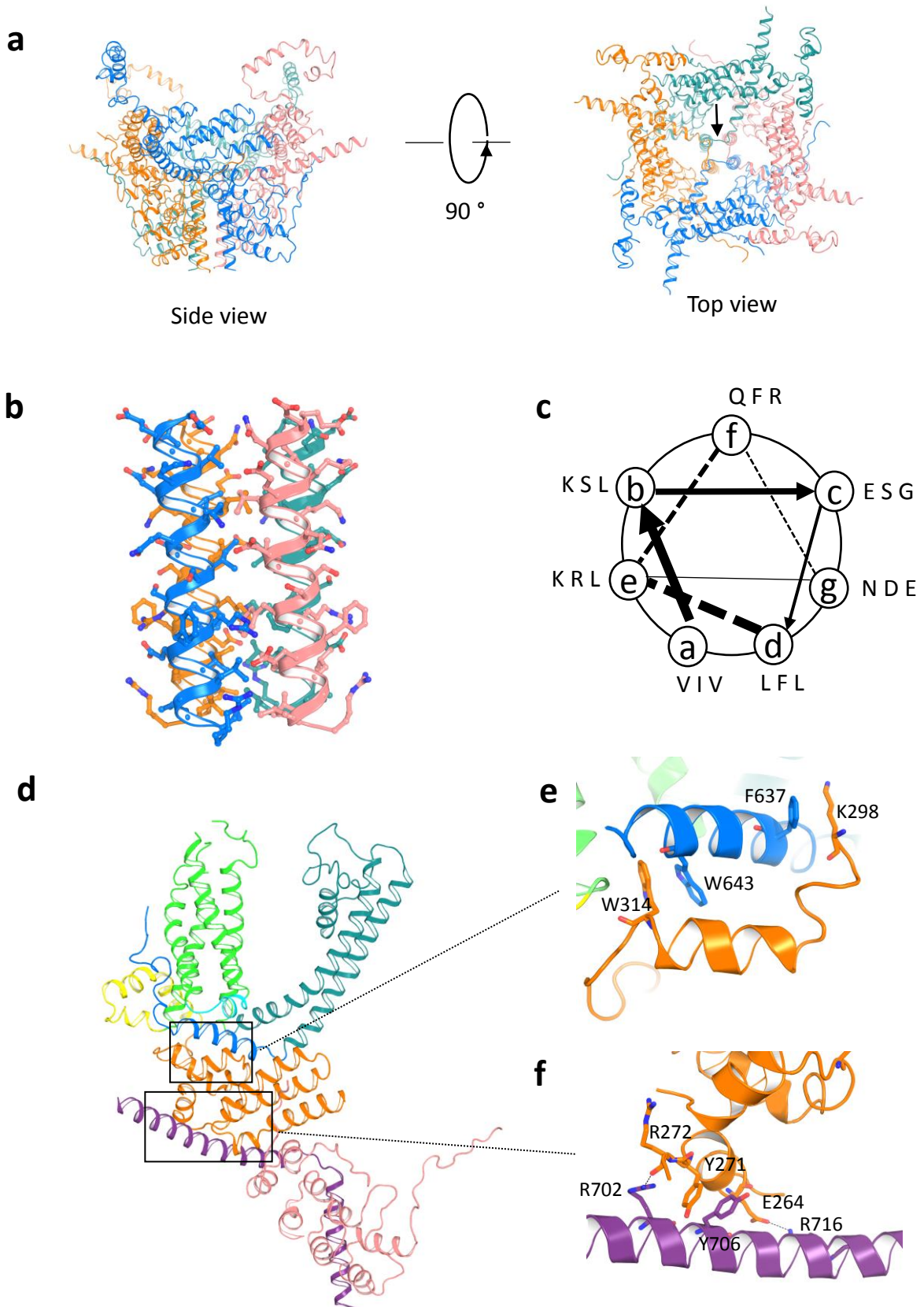


**Figure 4.**

